Integrating Human-Like Impedance Regulation and Model-Based Approaches for Compliance Discrimination via Biomimetic Optical Tactile Sensors

Giulia Pagnanelli , *Graduate Student Member, IEEE*, Lucia Zinelli , *Student Member, IEEE*,
Nathan Lepora , *Member, IEEE*, Manuel Catalano , *Member, IEEE*, Antonio Bicchi , *Life Fellow, IEEE*,
and Matteo Bianchi , *Member, IEEE*

Abstract—Endowing robots with advanced tactile abilities based on biomimicry involves designing human-like tactile sensors, computational models, and motor control policies to enhance contact information retrieval. Here, we consider compliance discrimination with a soft biomimetic tactile optical sensor (TacTip). In previous work, we proposed a vision-based approach derived from a computational model of human tactile perception to discriminate object compliance with the TacTip, based on contact area spread computation over the indenting force. In this work, we first increased the robustness of our vision-based method with a more precise estimation of the initial contact area condition, which enables correct compliance estimation also when the probing direction is other than normal to the specimen surface. Then, we integrated within our validated framework the mechanisms of internal muscular regulation (co-contraction) that humans adopt during object compliance probing, to maximize the information uptake. To this aim, we used human co-contraction patterns extracted during object softness probing to control a Variable Stiffness Actuator (that emulates the agonistic-antagonistic behavior of human muscles), which is used to actuate the indenter system endowed with the TacTip for object compliance exploration. We found that our model-based approach for compliance discrimination, fed with more precisely estimated initial conditions, significantly improves with the human-inspired impedance regulation, with respect to the usage of a rigid actuator.

Index Terms—Force and tactile sensing, perception for grasping and manipulation, soft sensors and actuators.

I. INTRODUCTION

HUMAN touch has remarkable perceptual capabilities due to a complex interplay of tactile mechanoreceptors, the human motor system, and the embodied mechanical intelligence of the human body. It is an active sense, with tactile receptors contributing to the control and perception of body movements. Purposeful exploration enhances information uptake through touch [1], while the mechanics of human skin play a key role in shaping human tactile perception [2]. Replicating these capabilities in robotic systems remains challenging due to the complexity of biological components. Biomimicry offers a promising approach to modeling the key elements of human touch through a mathematical language that can be translated into artificial systems. To reach this goal, both the computational models and the embodied intelligence of human touch perception should be taken into account [3]. The design of soft optical tactile sensors [4], [5], [6], [7] has marked a significant leap forward in creating machines capable of experiencing touch akin to humans. These sensors, often inspired by the human skin's characteristics, utilize innovative materials like rubber membranes filled with gel to emulate the biological tactile qualities of human fingertips. Among them, it is worth mentioning the TacTip, which is a soft biomimetic optical tactile sensor designed to mimic the human fingertip's tactile capabilities [4], [8].

Between the functionalities of touch, the ability to perceive object compliance–its perceived softness or stiffness–stands out as particularly important. This skill enables humans to navigate complex environments, manipulate delicate objects, and interact more naturally with the world. Compliance perception

is primarily driven by the sense of touch, even though it is influenced by multiple sensory inputs [9]. Specifically, tactile information gleaned through the skin's deformation during touch interactions emerges as the primary driver in our perception of object softness [10]. In the pursuit of artificially replicating the human touch's ability to distinguish object compliance, the integration of tactile sensors with deep learning techniques emerges as a promising methodology in the field. Indeed, the synergy between optical tactile sensors and deep learning has led to a new paradigm where machines can interpret tactile information and adapt their actions based on touch feedback. This capability extends beyond mere object recognition to the perception of object softness [11], [12], [13], enabling robots to handle fragile items delicately or exert appropriate force in various tasks. The applications of these systems are vast, spanning various domains such as manufacturing, healthcare, prosthetics, and telerobotics. However, despite the progress made, machine learning techniques face challenges. While they successfully bypass the need for explicit sensor-object interaction models, they are constrained by the quality and complexity of the data required for effective training [14]. Furthermore, the way the information is encoded is usually far from the computational mechanisms underpinning human tactile perception, making hard the possibility to convey such information back to the human operator, e.g., in telerobotics applications, in an easily understandable manner. These limitations can impede the system ability to generalize and comprehend the nuances of tactile interactions across various scenarios, including human-robot interaction.

In our previous work [15], we proposed, for the first time, a model-based strategy based on a computational model of human tactile perception to estimate object compliance using the TacTip sensor. Our methodology is rooted in the contact area spread rate (CASR) paradigm [16], according to which the contact area growth, (with respect to the indenting force), on the fingertip during object probing is larger with more compliant objects.

We accounted for two key elements of the biomimetic pipeline: 1) sensor design; and 2) computational models of human touch. However, we did not fully grasp and consider the active role of human embodied intelligence regulation, i.e., the control of the human muscular skeletal state that actively determines and shapes our perception. This is evident in several sensory modalities, like vision [17], and in touch, where exploratory procedures, i.e., purposeful stereotyped hand movements that humans tend to perform to maximize the information uptake over given tactile properties [18], represent a notable example. Other studies also revealed that touch is strongly connected to an individual's ability to interpret sensory information and determine the most appropriate biological motor control strategy and body state regulation [19].

In [20], the authors reported that humans, when probe soft deformable objects, tend to control the co-contraction level of antagonistic muscles to vary the mechanical impedance of fingers. In this manner the perceptual capabilities are increased at a kinesthetic level (acting on proprioceptive sensors located at muscle spindles) and at a cutaneous ones (acting on skin mechanoreceptors at different depths). Such an internal

impedance control was proven to play a significant role not only in biological tactile perception but also in its robotic counterpart [21], [22]. In these investigations, the focus was on the flexo-extension of the index finger, which is mainly actuated via the metacarpophalangeal joint actuated by two antagonistic forearm muscles, i.e. the Flexor Digitorum Superficialis (FDS), and the Extensor Digitorum Communis (EDC), In particular, the impedance of the joint increases with the simultaneous increase in activity of these two muscles (co-contraction).

Building upon this evidence, we explored the potential to enhance our biomimetic approach for compliance discrimination by incorporating the human muscular co-contraction strategy during object exploration, i.e., human-inspired embodied intelligence regulation. Of note, while with nonoptical tactile sensors, there are approaches that focus on force distribution measurements to control sensor deformation by regulating the exploratory procedure for compliance estimation [23], our approach focuses on optical contact area spread estimation under varying indenting force, i.e., the focus is on force variation (dF). Furthermore, assuming the validity of Hertz's theory, we consider homogeneous characteristics at contact.

II. CONTRIBUTION

This article proposes two key improvements to our previous approach [15] by addressing two main points. First, we generalize the outcomes of our model-based method during the exploration of specimens with different slope values with respect to the indenting direction. In [15], the results of compliance discrimination significantly deteriorated when the indenting direction of the probe endowed with the TacTip was different from the normal to the surface of the explored object. As the contact area is mathematically represented as the solution of a differential equation, our intervention involves a more precise fitting of the initial condition, proposing a new vision algorithm. It processes the visual information collected via the TacTip to refine the estimation of the initial contact area condition. Since the initial condition translates into the value of the area upon first contact, we improve the vision algorithm proposed in the previous work to estimate the initial area. The refined algorithm now accurately estimates the initial contact area for different angular orientations of the probing axis endowed with the TacTip with respect to the object surface. Second, and more importantly, we advance our research by integrating human muscular co-contraction strategy during object exploration to maximize object compliance discrimination. To achieve this, we gathered comprehensive data of human electromyography (EMG) signal profiles recorded from multiple participants engaged in object exploration for compliance recognition. Analyzing these EMG signals allowed us to extract the muscular impedance patterns employed by participants as they explored objects with varying degrees of compliance. We mapped the human impedance profiles onto the control of a variable stiffness actuator (VSA), which mimics the agonistic–antagonistic behavior of human muscles [24], to replicate human-like muscular behavior during specimen indentation with the TacTip sensor, combined with the model-based approach originally proposed in [15]. The findings

from our experiments highlight the significant advancements achieved by integrating the human co-contraction strategy in our biomimetic approach. The notable improvement is evident not only in the considerable reduction of compliance estimation errors, even during contacts along axes not normal to the object surface, but also in the heightened sensitivity of the mechanism to distinguish between various levels of object compliance. The successful replication of the human co-contraction strategy emerges as a pivotal element, playing a crucial role in enhancing both the adaptability and precision of our robotic system when faced with the diverse compliance characteristics encountered during object exploration. These results affirm the efficacy of our biomimetic approach and underscore its potential for addressing the intricacies of real-world applications with greater finesse. Indeed, although other approaches in the literature rely on vision-based methods for stiffness estimation, e.g., [25], they lack biomimicry because they do not take into account computational models of human tactile perception and their integration with soft biomimetic sensors. In summary, this article presents significant advancements in our biomimetic approach by refining the initial contact area estimation with a novel vision algorithm and integrating human muscular co-contraction strategies into robotic control. These improvements address previous limitations and result in more accurate compliance discrimination, even for contacts at nonnormal angles. Our findings demonstrate that emulating human-like muscular behavior enhances the precision and adaptability of robotic systems in object exploration, underscoring the potential of our approach for real-world applications.

III. Background and Problem Definition

This research aims to enhance our previous work, where we introduced a model-based approach grounded in human perceptual mechanisms for discriminating object compliance utilizing the TacTip tactile sensor. Our model pries upon the CASR paradigm [16], which demonstrated that the growth of the contact area between the fingertip and the probed object with respect to the indenting force is larger the softer (i.e., the more compliant) the object is. CASR stands with respect to the tactile flow model [26]—see the section below, as the time-to-contact estimation stands with respect to optical flow. In our previous work, we estimated CASR by computing the optical flow from TacTip images collected during the indentation process of silicone specimens with various compliance levels, thus enabling the estimation of the compliance characteristics of unknown objects. Moreover, we demonstrated the capability to differentiate between different compliance levels, which decreases while approaching the object along directions that deviate from the normal one referred to the specimen surface.

In this work, we present a refined method for more accurately estimating the initial contact area by improving the CASR assessment for different indenting directions, and replicating human co-contraction behavior during object exploration for softness discrimination.

A. Model-Based Biomimetic Approach

The approach developed for discerning object softness remains the same and relies on the soft biomimetic optical tactile sensor, the optical flow computation from sensor imagery, and the CASR.

The TacTip sensor, designed to mimic the layers of glabrous skin, comprises an outer rubber layer and an inner elastomer gel filled with rigid nodular marked pins [4], [8], allowing detecting touch exclusively through shear strain and collecting information about surface deformation.

The concept of optical flow delineates the apparent motion of objects in a visual scene due to an observer's movement relative to the scene. Representing the distribution of apparent velocities of brightness patterns in an image [27], [28], it significantly contributes to locomotion control, perceiving movement, and distance, in various domains, including robotics [29], [30], [31]. In our previous work, we employed the dense method proposed by Horn and Schunck [32] to evaluate optical flow from TacTip camera frames. This method imposes velocity constraints to ensure correct optical flow estimation, allowing smooth variation in brightness pattern motion across the image [33], [34], [35], [36].

The CASR paradigm proposed in [26] demonstrated that areas on the fingertip with equal Merkel corpuscle activation, known as Iso-Strain Energy Density contours, expanded outward as probing force increases, offering insights into probed objects compliance. As the apparent motion of iso-brightness contours can be described by the optical flow model, the expansion of the iso-strain contours can be accounted by the tactile flow model, which allows to explain haptic counterparts of common visual illusions. In [15], we used the optical flow to approximate the tactile flow, by linking the iso-brightness patterns expansion due to the pins' movement to stress-strain distributions over the TacTip surface during contact.

Furthermore, given the similarity between this expansion and the radial patterns of brightness contours used in vision for estimating an object collision time w.r.t. the camera plane, our work in [15] drew on the time-to-contact theory proposed in [37]. We applied this theory to assess the area's rate of change based on image divergence. Specifically, we redefined the theory in the force domain, shifting the focus from time to force. This approach allows us to analyze how the area changes over increasing indenting force, to devise information on object compliance.

Based on that, we finally evaluate the contact area corresponding to the probing force F_i at the ith frame as

$$A_{c_i} = A_{c_0} \exp(\mathscr{D}\text{cum}Fi). \tag{1}$$

Here, Ac_0 represents the initial area calculated under the TacTip's static condition through a vision algorithm and $\mathscr{D}\text{cum}$ is the summation of the divergence of the dense optical flow in a frame sequence. Note that, as demonstrated in [15], (1) derives from the results of Cipolla and Blake [37], i.e., from the definition of the optical flow divergence equal to the cumulative divergence of the optical flow multiplied by the area:

$\frac{dA_c}{dF} = \iint_{A_c} \mathscr{D} \, dA = A_c \mathscr{D}_{\text{cum}}$. After obtaining the contact area value, we computed the CASR, i.e., $\frac{dA_{c_i}}{dF_i}$, at frame i using the equation

$$\frac{dA_{c_i}}{dF_i} = \sum_{j=1}^{i} \frac{A_{c_j} - A_{c_{j-1}}}{F_j - F_{j-1}} \qquad (2)$$

considering $F_0 = 0$. Consequently, the computed CASR for the entire frame sequence was derived using (2) with $i = number\ of\ frame$. The CASR estimation allows the differentiation of softness levels of the explored objects. Higher CASR values indicated softer materials.

However, the accuracy of the obtained results in terms of compliance estimation error significantly worsened as the contact direction moved away from being perpendicular to the object's surface. Upon a thorough analysis of the prior results, we noted that employing the same initial condition to solve the differential equation, irrespective of the approach direction towards the object, fails to yield optimal solutions. Indeed, the more inclined the axis defining the approach towards the object is in relation to the normal axis of the object surface, the smaller the initial contact area becomes. To establish a more appropriate initial condition considering the actual sensor surface involved in the initial contact, within the previously proposed pipeline, we suggest an enhancement to the vision system.

B. Human Inspired Impedance Regulation

As widely mentioned in [15], the model-based biomimetic approach only exploits the cutaneous cue. Here, we put forward delving into the prospect of integrating a kinesthetic element into our framework to increase the sensitivity of our model. In support of that, in [20] and [21], authors demonstrated that humans act on muscle stiffness control to enhance object compliance perception [38]. Our approach for kinesthetic cues exploitation aims to replicate the muscular impedance involved by humans in soft object probing. We propose to substitute the actuation system used in our previous work [15], based on a dc motor, commanding the indentation of the TacTip over the compliant specimen, with a suitable variable stiffness actuator, i.e., Qbmove [39], [40].

Similar to the case of natural musculoskeletal systems, Qbmove allows moving the output shaft while also modulating the mechanical stiffness of the shaft itself. The Qbmove structure presents two motors connected to the output shaft through linear springs, implementing a nonlinear elastic transmission. This configuration results in a mechanical implementation of the antagonistic principle, where two muscles work on a natural joint. The system inputs are the semisum and semidifference of the motor position for r and c, respectively. In order to control the motors angles θ_1 and θ_2 according to the reference inputs r and c, a low-level controller is constructed in the onboard controller (see Fig. 1). Operatively, the desired position of the output shaft is defined as $(\theta_1 + \theta_2)/2$ while the desired stiffness as $(\theta_1 - \theta_2)/2$. When the motors rotate in opposite directions, the springs become loaded, changing the working point and, consequently, the resulting stiffness. In the absence of
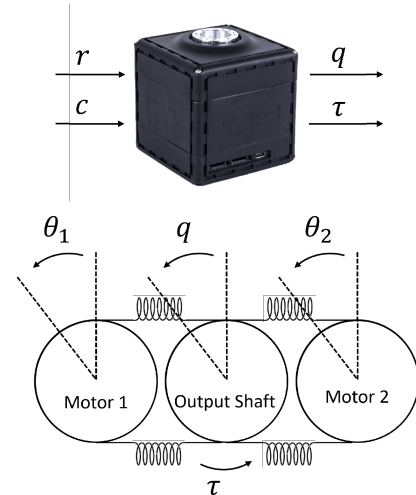

Fig. 1. Qbmoves actuator design and parameters.

an external load, this movement does not affect the output-shaft equilibrium position since the two transmission systems have the same properties. The behavior that arises is consistent with the widely recognized equilibrium point theory of Feldman [41], on human motor control. The described work principle can be used to replicate the human co-contraction activity involved in several tasks. This is done by mapping onto the actuator stiffness the muscular impedance profiles defined as the sum of the agonistic–antagonistic activity [42].

IV. METHODS

A. Improved Vision Algorithm

In this section, we propose a new vision algorithm that aims to refine the estimation of the initial contact area by leveraging information from the first two frames captured by the TacTip sensor.

Initially, in [15], the algorithm considered the area of a circle with a radius determined by the farthest pin from the central one as the initial condition to solve (1).

The new algorithm (Algorithm 1) utilizes data from the frame representing the static condition of the TacTip surface, and from the initial frame, representing the first contact, to enhance the accuracy of the definition of the initial contact area. It processes each frame to extract pixel coordinates corresponding to the center of each pin. This task was accomplished by applying shape and color masks to isolate and identify the pins individually, allowing for the delineation of their contours and their respective centroids. The next step involves pairing the centroids obtained from both frames. This was achieved by sorting the pin coordinates and matching centroids between the two images. Then, the algorithm identifies and saves centroid pairs displaying displacement between the initial and subsequent frames. For each pair of saved centroids, it exclusively utilizes the coordinates from the first frame to establish the center point of a hexagonal shape. The choice of a hexagon was motivated by the arrangement of the pins on the TacTip surface, as this shape
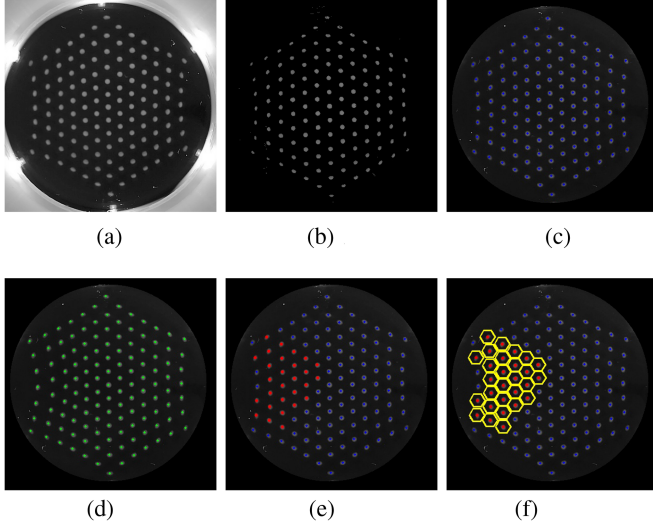
Fig. 2. Visualization of the vision algorithm for A_{c_0} estimation. (a) Frame. (b) Shape and Color Mask. (c) Contours and Centroids 1. (d) Contours and Centroids 2. (e) Selected pins. (f) Hexagon for A_{c_0}.

offered better coverage of the area of interest, as depicted in Fig. 2(f). To evaluate the area of one hexagon, knowing the radius r_h of the hexagon and the regularity of the defined polygon, we first evaluate the apothem a and the side l in pixel as

$$a = r_h \cos 30°$$
$$l = 2r_h \sin 30°. \tag{3}$$

Then, we project the pixel value of the apothem and side to their actual values in mm by exploiting the distance information from the depth d sensor expressed in mm and the undistorted camera matrix (intrinsic parameters)

$$k = \begin{bmatrix} f_x & 0 & c_x \\ 0 & f_y & c_y \\ 0 & 0 & 1 \end{bmatrix} \tag{4}$$

with f_x and f_y focal lengths, and c_x and c_y the principal point offsets, all expressed in pixels

$$a_{\text{mm}} = \frac{a \cdot depth}{f_y} \quad l_{\text{mm}} = \frac{l \cdot depth}{f_x}. \tag{5}$$

Then, the area of one hexagon in mm^2 is evaluated as $A_{hex} = 6 \cdot l_{\text{mm}} \cdot a_{\text{mm}}/2$ and the total initial area as $A_{c_0} = n \cdot A_{hex}$, with n the number of selected pins.

Fig. 2 shows the main result obtained with the new vision algorithm. In particular, it refers to the case in which the angle between the axis of contact direction and the normal to the surface is about $45°$.

B. Human-Like Compliance Exploration

This section describes the experiments conducted on 14 right-handed subjects (5 Male and 9 Female, Age mean $\pm$ SD: 30.5 ± 11.31) without any hand or wrist injuries. The experimental procedures were approved by the Committee on Bioethics of the

---

Algorithm 1: Initial Area Estimation.

Step 1: Apply masks to the first and second frames for pins detection
$frame_1 \leftarrow file.TIFF[0]$
$frame_2 \leftarrow file.TIFF[1]$
$mask\_circle = cv.circle(mask)$
$mask\_color = cv.inRange(frame, low\_color, upp\_color)$
$frame \leftarrow frame + circle\_mask + color\_mask$

Step 2: Find pins contours and respective centroids for both frames
$contours_{frame_i}, hierarchy_{frame_i} = cv.findContours(frame_i)$
for i in range $(0, \text{len}(contours_{frame_i}))$ **do**
  $c = contours[i]$
  $area = cv.contourArea(c)$
  $moments = cv.moments(c)$
  if moments["m00"] != 0 **then**
    $cX = int(moments["m10"]/moments["m00"])$
    $cY = int(moments["m01"]/moments["m00"])$
  else
    $cX, cY = 0, 0$
  $centroid_{frame_i}.append(cX, cY)$

Step 3: Evaluate pin displacement between two frames
$distance = 0$
for i in range $(\text{len}(centroid_{frame_1}))$ **do**
  for i in range $(\text{len}(centroid_{frame_2}))$ **do**
    $distance = abs(centroid_{frame_1} - centroid_{frame_2})$
    if $distance > 2$ **then**
      $signpin.append(centroid_{frame_1})$
Step 4: Evaluate the initial Area as the sum of the hexagon area
$A_{c_0} = 0$
for i in range $(\text{len}(signpin))$ **do**
  $A_{hex} = $ area of hexagon centered in $signpin[i]$
  $A_{c_0} = A_{c_0} + A_{hex}$

University of Pisa—Review No. 30/2020. Participants provided their informed consent to be enrolled in the study. The sample size derived from a power analysis we performed, considering that each participant must perform ten exploratory movements per specimen, having a power $1 - \beta$ of around 80%, error probability α equal to 0.05, and an effect size f equal to 0.25. The experiments aim to evaluate the human forearm muscular co-contraction, in terms of muscular impedance, while palpating five specimens with varying degrees of compliance. In addition, we outline how we reproduce the muscular impedance with the Qbmove VSA [39], [40].

Our investigation specifically targets the flexion movements of the index finger, controlled by the metacarpophalangeal joint. Previous studies [43], [44] have demonstrated that the impedance of this joint can be modulated by activating two
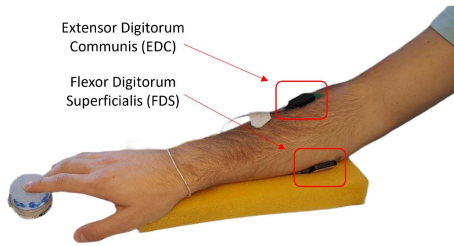
Fig. 3.   EDC and FDS EMGs collection during silicon palpation.

opposing forearm muscles, i.e., the FDS and the EDC. Particularly, the impedance of the joint increases with the simultaneous activation of the two involved muscles. We quantify this phenomenon by analyzing the surface electromyography (EMG) measurements of the muscles collected during the experimental phase. During the experimental session, subjects were seated comfortably, resting their dominant forearm on soft support over a laboratory desk. The forearm skin was thoroughly cleaned, and two Delsys Bagnoli EMG electrodes were affixed to capture the electromyographic signals of the FDS and EDC muscles at 1000 Hz. We asked the participants to palpate several specimens (two in the training phase and five in the real experiment) with different compliance levels using the index finger (Fig. 3).

These specimens were created by combining varying amounts of Sylgard 184 silicone in order to have various softness. The palpation continued until an indentation force of 7 N, along the vertical axis of the specimen (F_z), was reached. A F/T sensor ATI Mini45, running at 1000 Hz with a cutoff frequency of 5 Hz, was placed under the specimen in order to measure the force applied during the palpation. Moreover, a suitable graphical interface was developed to facilitate the correct execution of the experiment. Specifically, this GUI displays "start" and "stop" commands for the participant and a force intensity bar with values ranging from 0 to 7 N. The intensity bar increases and decreases respectively with the increase and decrease of the indentation force applied by the participant. In addition, the bar is colored green when the force increases and red when it decreases, as compliance discrimination via CASR requires that the force monotonically increases. Therefore, the red color serves as a warning, especially during the training phase. During this phase, participants practiced applying increasing indentation forces of up to 7 N on two specimens with varying compliance levels (different from the five used in the experiments). Exploiting the same GUI, they were instructed to press on the specimen when the "start" command appeared on the GUI and to lift their finger when the "stop" command was given. This phase is really important since allows participants to familiarize themselves with the procedures and equipment, ensuring they understood the correct starting conditions and preventing premature force application before the experiment begins. Furthermore, the height of the chair was adjusted based on the height of the participant to ensure that their forearm was completely sustained by the soft support. This condition was verified by the experimenter before each trial. For each specimen, five trials were conducted.

Throughout the experiment, subjects replicated the same movement on five specimens, S_1, S_2, S_3, S_4, and S_5, presented in a random order, distinct from those used during the training phase, with stiffness equal to $\kappa_{S_1} = 7.63$ N/mm $> \kappa_{S_2} = 5.32$ N/mm $> \kappa_{S_3} = 3.35$ N/mm $> \kappa_{S_4} = 3.12$ N/mm $> \kappa_5 = 1.11$ N/mm, for each of which they performed ten repetitions. As described in [15], the stiffness of each specimen was evaluated by exploiting the previous version of our indenter apparatus with the TacTip sensor replaced with an ABS smooth plate as a tactile tool to perform indentation tasks along the vertical axes. We indented each specimen five times, recording the indentation force and the tool position. We used the collected data to estimate the stiffness coefficient of each specimen through the linear Hooke model by fitting prefiltered force (a moving average filter with a window of five elements, a cutoff frequency of around 5 Hz, and a delay of 0.5 s) and indentation values obtaining a worst adjusted R-squared of 0.882. The raw EMG signals collected from both EDC and FDS muscles were preprocessed by applying the rectification and smoothing method with the Root-Mean-Square (RMS) processing. In particular, we used a second-order Butterworth band-pass filter with a range of $[10 - 500]$ Hz to minimize high-frequency noise and eliminate steady and slow-changing behaviors. After, we rectified the resulting signal and extracted the envelope using a 50th-order FIR low-pass filter with a cutoff frequency of 20 Hz [45]. For each trial, we considered contact forces ranging from 0.5 to 7 N [46], and we extracted the co-contraction activity, e.g., muscular impedance, by summing the EMG signals from this muscle pair [42]. In the perspective of mapping this impedance profile onto the VSA for human co-contraction reproduction, the co-contraction activity collected for each trial was also fitted using the following logarithmic equation:

$$v_{emg} = a + b \cdot \log(F_z) \tag{6}$$

where v_{emg} represents the electromyographic signal value corresponding to a specific force value F_z, and a and b are parameters dependent on the fitted data. The worst adjusted R-squared is equal to 0.832.

Considering having for each subject, a group of ten fitted curves for each specimen, i.e., 50 curves for each subject, 700 curves in total, for the statistical analysis we took into account the coefficient b of each curve group, opportunely clustered in 70 clusters, i.e., $B_{i,j} = [b_1, \ldots, b_{10}]$, with $i = 1 : 14$ number of subjects and $j = 1 : 5$ number of specimens.

According to the one-sample Kolmogorov-Smirnov test, each cluster has a Gaussian distribution. Therefore, we employed a parametric ANOVA test with LSD post-hoc correction for two purposes: First, to statistically confirm the absence of significant differences between subjects' EMG profiles related to the same specimen, and second, to assess the differences between impedance muscular profiles in distinguishing different silicone specimens, for each subject. The first analysis confirmed the null hypothesis, indicating that no statistically significant differences exist between subjects. Otherwise, for all fourteen subjects, the statistically different muscular profiles were associated with S_1,
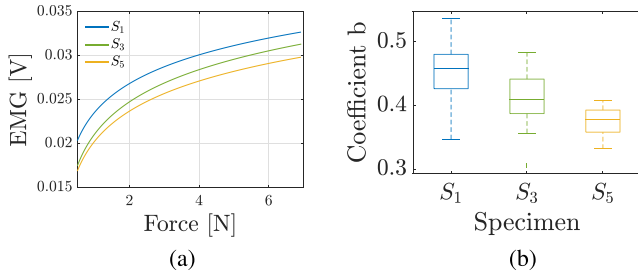
Fig. 4. Evaluation of the human muscle co-contraction activity. (a) Average trend of muscle co-contraction of a random subject. (b) Boxplot of coefficient b.
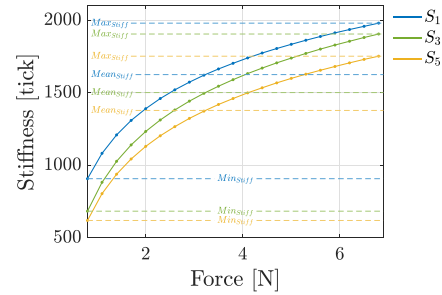

Fig. 5. Mapping the muscle co-contraction on the VSA stiffness. The dynamic trends mapped onto the VSA in the human-like experiment with modular stiffness referred to each specimen are color-coded, respectively, S1 in blue, S3 in green, and S5 in yellow. The dotted lines represent the constant values of minimum, mean, and max stiffness mapped onto the VSA in the human-like experiment with constant stiffness. Scatter dots represent the stiffness values mapped onto VSA.

S_3, and S_5, exhibiting a p-value of 0.0391 in the most conservative scenario. For each subject, we examined the average trend of human co-contraction activity related to each specimen, calculated as the mean of the ten post-processed signals. Considering no statistical differences between subjects and that we have ten repetitions for each specimen and each subject for an amount of 700 sample data, we opted for reporting one figure that shows the mean EMG behavior obtained for each statistically distinct specimen across all repetitions of an exemplary participant. Fig. 4(a) represents the average trend of the fitting of muscle co-contraction activity for the silicones S_1, S_3, and S_5, whereas Fig. 4(b) illustrates the boxplot of the fitting coefficients b (the three considered samples are defined by putting together the 10 b coefficients obtained for each considered specimen across the ten repetitions). Both plots show that muscular co-contraction activity is strongest with the harder silicone, S_1, and gradually decreases towards the softer silicone, S_5.

Since no difference exists between subjects we considered the average trends obtained for each specimen from the exemplary participant and shown in Fig. 4(a), and translated them into the VSA's stiffness through

$$k_{vsa} = p_1 \cdot v_{emg_{mean}} + p_2 \qquad (7)$$

where $v_{emg_{mean}}$ represents the mean value of the EMG signal evaluated for force intervals of 0.3 N, and p_1 and p_2 are parameters derived from the linear mapping between the range of $v_{emg_{mean}}$ values and the stiffness range of k_{vsa} based on the minimum and maximum values of both variables. This ensures changing the VSA stiffness opportunely. Equation (7) aligns the minimum co-contraction value with 20% of the actuator maximum stiffness and the maximum co-contraction value with 80% of the actuator maximum stiffness (Fig. 5). These thresholds are selected to guarantee a safe work range for the VSA. Considering the principle of work of Qbmove described in Section III-B we control the actuator by setting the stiffness, at steps of 0.3N, and the desired output shaft position, respectively, as

$$\frac{\theta_1 - \theta_2}{2} = k_{vsa} \qquad \frac{\theta_1 + \theta_2}{2} = pos_{des} \qquad (8)$$

where θ_1 and θ_2 are the positions of motor 1 and motor 2 and pos_{des} is defined by a linear equation ensuring a velocity along the vertical axis around 5 mm/s.

Moreover, for the sake of completeness of analysis, considering the same linear relationship (7), we extracted the minimum, mean and maximum values of each muscular impedance curve and mapped them on the VSA as constant stiffness (Fig. 5).

The first mapping enables the investigation of the efficiency in fully utilizing the dynamic stiffness range when exploring the object like humans do in palpation activities.

The second mapping enables exploration of the disparities in object stiffness discrimination resulting from employing constant impedances set to the minimum, maximum, and mean values of each curve, respectively. Through this investigation, we also assess whether utilizing an average muscle impedance value yields comparable results to those achieved by leveraging the entire impedance curve.

V. EXPERIMENTS

This section describes the experiment performed as in [15] with (1) the new vision algorithm and (2) those performed with the new framework with the human-inspired co-contraction strategy. We investigated three alternative contact directions $0°$, $30°$, and $45°$, currying out ten repetitions for each specimen and angle. More precisely, we considered surface angles of $30°$ and $45°$ for (1) and of $0°$, $30°$, and $45°$ for (2). More specifically, regarding human-inspired impedance regulation, in the case of the exploration with constant stiffness, we investigate only the normal contact direction, i.e., $0°$, sufficient for investigating the differences between the two strategies implemented with VSA. Indeed, while the improvement of the vision algorithm significantly affects the case of the inclined surface, the integration of the human co-contraction strategy affects all situations. Of note, the experiments aiming at evaluating VSA-enabled exploration were conducted using the modified vision algorithm.

A. Experimental Setup

The vision algorithm validation experiment was performed by using the apparatus outlined in [15]. Briefly, the apparatus include the following:
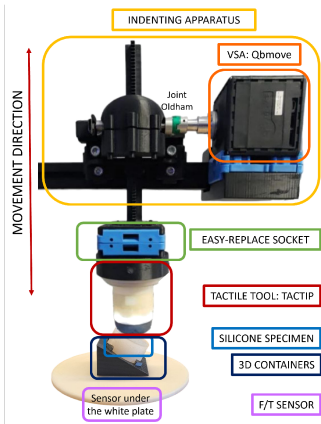
Fig. 6.   Modified apparatus with VSA for human-like experiments.

1) a motor-driven cogwheel system that vertically moves a rigid ABS rapid prototyping printed support to host the TacTip sensor. The sensor was actuated by a Maxon DCX8 dc brushed motor with a planetary gearbox GPX8 35:1, power supplied at 12 V and controlled by a qbrobotics board [39];

2) an Auster Microsystem AS5045 encoder with a 12-bit resolution was used to compute the motor position;

3) a 3-D printed circular plate fixed under the moving frame to hold the tested specimen;

4) an ATI Mini45 sensor, with a resolution of 0.0625 N, for measuring vertical forces, fixed under the plate for measuring vertical forces.

For the experiment involving the Qbmove, we made slight modifications to this existing setup (Fig. 6). Specifically, we designed a VSA support in ABS using rapid prototyping techniques, and a shaft connector through CNC machining, to link the output shaft of the VSA to the preexisting cogwheel system. A Oldham joint was used to connect the motor output shaft and the shaft of the cogwheel system. This allows for avoiding possible misalignments, enabling a linear transmission of the stiffness from the VSA to the sensor support. In the experiments with the VSA, the new vision algorithm was used for the initialization of the CASR estimation procedure.

B. Experimental Procedure

Experiments consist of indenting with the TacTip sensor, along the chosen contact direction, specimens with different levels of compliance by applying incremental probing force. We performed the experiments considering specimens S_1, S_3, and S_5, which showed statistically significant differences in muscle impedance profiles across the subjects. Then we used S_2, from now on denoted as S_{new}, as a new specimen for the stiffness estimation error evaluation. Custom-designed and 3-D printed containers (Fig. 7) [47] were employed to change the surface inclination of the specimen to test the proposed approach along different exploration directions.

For each specimen and considered surface, two different approaches were used: the first one, which we refer to as the
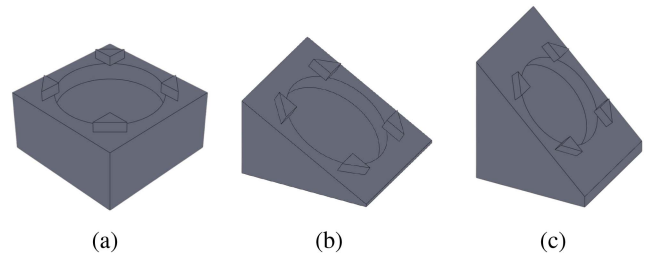

Fig. 7.   Support to perform experiments considering several angles between axis normal to the surface and contact direction. (a) Indentation with $0°$. (b) Indentation with $30°$. (c) Indentation with $45°$.

high-stiffness approach, exploits the old setup involving a dc motor, so does not consider the variable stiffness; the second, which we refer to as the human-like approach, uses the new framework involving the VSA controlled with human muscular impedance mapping. Moreover, the human-like approach, in turn, involved two kinds of approaches. In the first, i.e., *modular stiffness*, the indentation task is performed by mapping onto the VSA the whole experimentally obtained human co-contraction profile. In the second approach, i.e., *constant stiffness*, the same task is carried out by mapping onto the VSA a constant stiffness equal to the minimum, maximum, and mean values of the human impedance profile. This resulted in a total of five experimental conditions for each specimen and each angle.

Each experimental repetition involved indenting the specimen placed on the rigid circular plate with the TacTip attached to the proposed mechanical system. During the indentation, which we can refer to as the loading phase, the speed of the tactile tool was maintained at 5 mm/s to remain within the elastic domain of contacts, where Hertz's theory is applicable. Slow loading rates ensure that stresses are in static equilibrium with external loads throughout the loading cycle, allowing the neglect of dynamic effects. Each indentation was carried out remaining in a predefined range of contact forces applied ranging from 0.5 N to a fixed threshold F_{max} chosen to align with normal loads associated with light touch perception in humans [48]. Indeed, we used the force information to define the state of the indentation; specifically, the lower bound reflects the instant at which the tactile tool comes into contact with the specimen, while the upper bound denotes the end of the trial. During each test, the tactile tool moved towards the specimen along the vertical axis until the top bound was reached, then returned to the starting point and waited for two seconds before beginning the next trial. Each trial involved saving raw and filtered contact forces, indices of saved TacTip camera frame, and the TacTip camera image sequence. The same custom double-thread C++ presented in [15] was used to manage the whole experimental procedure and for the data acquisition. To sum up, the main thread determines the motor desired position (and stiffness when QBmove was used to act the TacTip) and saves force data and camera image frame number at a frequency of 200 Hz. The high-priority thread employs a moving average filter with a window of five elements, a cutoff frequency of around 5 Hz, and a delay of 0.5 s for force filtering. The low-priority thread saves TacTip grey-scale 300×300 pixel

camera images at a rate of 20 Hz. It is worth noting that, to perform the experiment with the human-like method, a position control strategy is not enough for the Qbmove. So, we applied the control strategy defined in Section III-B to set both stiffness and shaft position, according to (8).

Finally, a similar custom `Python` module [15], opportunely modified with the new vision algorithm, was used to implement and test the proposed approach with the new evaluation of the initial condition. This module used the collected and postprocess data to evaluate dense optical flow between consecutive frames (retrieved from the saved image sequence) and its divergence, estimate the initial area, and compute the CASR. Note that the hysteresis effects due to the TacTip deformable membrane are discarded since we considered only the indenting (loading phase) for CASR computation.

VI. RESULTS

This section presents the results obtained after analyzing the data collected during the experiments. First, we show the outcome of the biomimetic model-based approach involving the indentation enabled by the dc motor (high stiffness) and the improved vision algorithm. Then, we report the results fetched by integrating the human-like actuation in the biomimetic proposed method together with the new vision algorithm. This way allows highlighting the role of both enhancements, i.e., new initial area estimation and human-like variable stiffness actuation, in reaching a whole improvement of the model-based approach in discriminating and estimating the object's stiffness.

A. Vision Algorithm Validation

To ensure consistency in the results obtained with the new vision algorithm, it is necessary to verify that the values of the initial area do not vary significantly with changes in the specimen and are statistically different with changes in the contact direction. For this analysis, we collected all the initial area values returned by the algorithm for each specimen and each considered contact angle. Considering each angle separately, we took three samples, each for every specimen, consisting of the ten initial area values. After confirming the non-Gaussian distribution of the samples, we applied the Kruskal-Wallis test, which resulted in accepting the null hypothesis in all three contact angle cases. The corresponding p-values are 0.51 for $0°$, 0.74 for $30°$, and 0.61 for $45°$. Subsequently, having verified the nonsignificant difference in the contact area with changes in the specimen while fixing the contact angle, we created three samples, each containing all the initial area values obtained for all three specimens at the same contact angle. We applied the Kruskal-Wallis test to these samples with subsequent Bonferroni correction, which resulted in rejecting the null hypothesis with a p-value of $3.1079e-05$ in the worst case. Fig. 8 shows the obtained statistical results of both analyses through boxplot visualization, while Fig. 9 highlights the difference in the initial area considering different angles and the decreasing of the area when the angle increases.

As force values are recorded at a frequency of 200 Hz, whereas TacTip images are captured at 20 Hz, multiple force data are
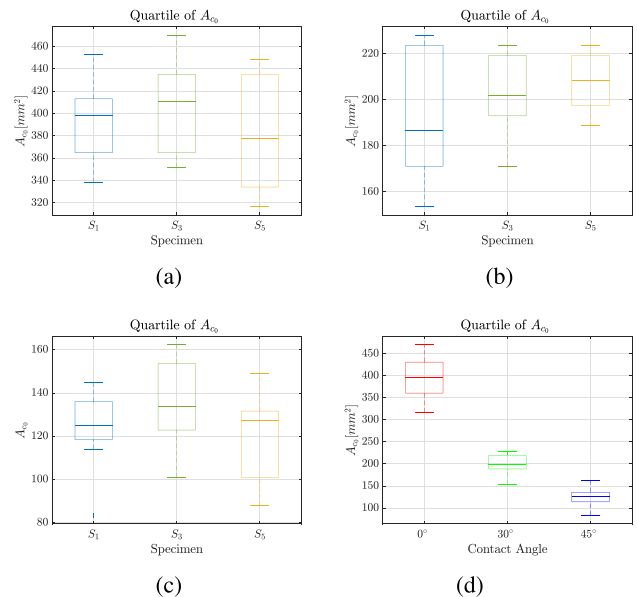

Fig. 8. Boxplot obtained from statistical analysis for algorithm's results validation. (a) Boxplot of A_{c_0} varying specimen at $0°$. (b) Boxplot of A_{c_0} varying specimen at $30°$. (c) Boxplot of A_{c_0} varying specimen at $45°$. (d) Boxplot of A_{c_0} varying angle.
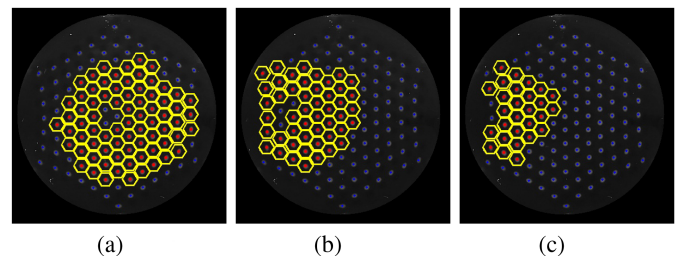

Fig. 9. Visualization of A_{c_0} correspondent to several angles. (a) A_{c_0} with $0°$. (b) A_{c_0} with $30°$. (c) A_{c_0} with $45°$.

collected for each saved image frame. Before validating the entire proposed model-based approach with the new algorithm, it is essential to resample these values. Due to the straightforward nature of the data, the chosen method involves considering the force value associated with each frame as the mean of all the force values saved relative to that specific frame.

At this stage, the proposed model with the new algorithm has been applied to all the experimental data to derive CASR values for each case. Initially, we validated the model through the Kruskal-Wallis test and Bonferroni correction resulting in a p-value of 0.0111 in the worst case, confirming that CASR values exhibit statistically significant differences with variations in the specimen. In addition, we verified that, for each selected contact angle, the contact area spread rate increases if the softness of the specimen increases (Fig. 10).

Later on, we applied the approach to data collected from a new and unknown specimen S_{new} performing ten experimental repetitions, as done for the other specimen, considering all three cases defined by the contact angles, to assess its CASR as the mean of the ten CASR values obtained from each collected data
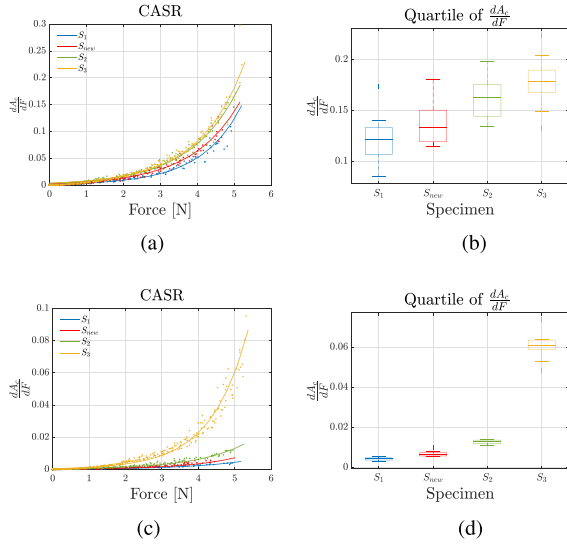
Fig. 10. S_{new} CASR discrimination based on the proposed model using the high-stiffness approach and considering different contact angles. Different specimens are color-coded, respectively, S_1 in blue, S_{new} in red, S_3 in green, and S_5 in yellow. (a) Raw data and fitting of $\frac{dA_c}{dF}$ at 30°. (b) Boxplot of $\frac{dA_c}{dF}$ at 30°. (c) Raw data and fitting of $\frac{dA_c}{dF}$ at 45°. (d) Boxplot of $\frac{dA_c}{dF}$ at 45°.

TABLE I
ESTIMATION ERRORS MADE IN THE EVALUATION OF $K_{S_{new}}$

Angle	Estimation Error old vision alg.	Estimation Error new vision alg.	Estimation Error new vision alg. and human-like palpation
0°	6%	–	3%
30°	25%	7%	3%
45°	28%	13%	4%

sequence. We verified that the specimen was correctly classified within the stiffness and CASR scale (Fig. 10) considering that we already characterized the objects that resulted in a stiffness of $\kappa_{S_{new}} = 5.32$ N/mm.

Subsequently, we identified the relationship between CASR and specimens' stiffness by fitting the previously obtained data. The resulting relation is described by an exponential equation with an adjusted R-squared of 0.8963 in the worst case. We used this relation to estimate the stiffness of S_{new} considering knowing only its CASR. The estimation error resulted equal to 7% and 13% for 30° and 45°, respectively (Table I).

B. Validation of Human-Like Approach

For a proper analysis of the exploration performed considering mapping the whole human co-contraction profile, we first need to resample the data collected during the experiment performed on S_1, S_3, and S_5. Indeed, since force values are recorded at 200 Hz while TacTip pictures are recorded at 20 Hz, we had many force data points per image frame. The strategy used is to consider the average force value for each frame. Then, to obtain the CASR values, we applied our proposed method with the data collected in each trial, considering the new estimation
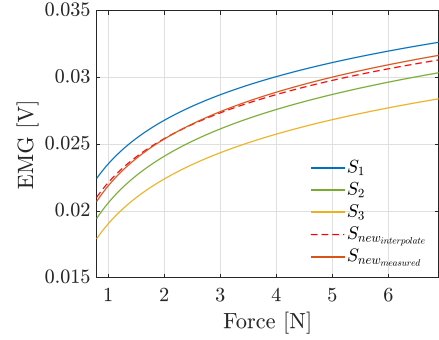

Fig. 11. Interpolated EMG profile for S_{new} (red dotted line) in comparison with EMG profiles from measurements.

area strategy. After verifying that our samples do not have a Gaussian distribution, we tested the three specimens, for each indentation angle, with the nonparametric Kruskal-Wallis test and subsequent Bonferroni correction to determine whether the CASR values showed statistically significant differences. The results revealed a rejection of the null hypotheses, with the worst p-value $= 0.0034$ for the surface at angles 0° and 30° and the worst p-value $= 0.0018$ for the surface at 45°.

Then, we evaluated also the CASR related to specimen S_{new}. In this case, the EMG profile mapped onto VSA is obtained through interpolation method that linearly combines the data from the original curves. First, we consider the coefficient of obtained logarithmic curves to evaluate the EMG profiles related to S_1, S_2, S_3 w.r.t. the same vector of force (generated considering 100 points between 0 and 7 N) to ensure uniformity. After aligning the curves, we introduced an interpolation factor, $\alpha \in [0, 1]$, which determines the relative contribution of each curve to the final result. Specifically, we considered a stiffness range of $[0 - 10]$ N/m, corresponding to 0% and 100%, respectively, mapped each specimen stiffness to its percentage value, and then normalized it within the range $[0, 1]$. Subsequently, we set $\alpha = 0.532$, i.e., the normalized percentage stiffness of S_{new}. With α determined, we generated the EMG profile for S_{new} by computing a weighted average between the EMG profiles of S_1 and S_3, that ensure S_{new} ling in between, with the weighting based on $1 - \alpha$ for S_1 and α for S_5. To enhance the robustness of our approach and increase confidence in the results, we compared the interpolated profile with real EMG data obtained from experimental measurements conducted with participants. The comparison resulted in an RMSE equal to 0.0002 V (Fig. 11).

Based on our prior knowledge that $K_{S_{new}}$ is less than K_{S_3} and higher than K_{S_1}, we verified that its CASR curve remains correctly between S_1 and S_3 curves. Fig. 12 illustrates the CASR trend for each specimen and the respective boxplot across all indentation angles. Plots highlight that the specimens are correctly discriminated based on the fact that the CASR values are higher the softer the object is. Moreover, both plots show the correct discrimination of the new specimen compliance level.

Based on the results, as done before, we derived the relationship between the evaluated CASR and known stiffness of S_1, S_3, and S_5 through exponential fitting that results in an
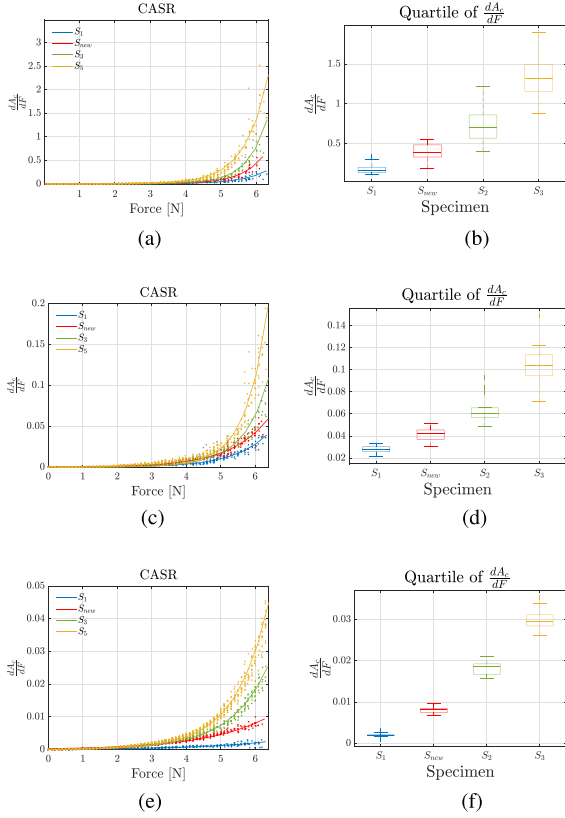
(a)

(b)

(c)

(d)

(e)

(f)

Fig. 12. S_{new} CASR discrimination based on the proposed model using the human-like approach and considering different contact angles. Different specimens are color-coded, respectively, S_1 in blue, S_{new} in red, S_3 in green, and S_5 in yellow. (a) Raw data and fitting of $\frac{\mathrm{d}A_c}{\mathrm{d}F}$ at $0°$. (b) Boxplot of $\frac{\mathrm{d}A_c}{\mathrm{d}F}$ at $0°$. (c) Raw data and fitting of $\frac{\mathrm{d}A_c}{\mathrm{d}F}$ at $30°$. (d) Boxplot of $\frac{\mathrm{d}A_c}{\mathrm{d}F}$ at $30°$. (e) Raw data and fitting of $\frac{\mathrm{d}A_c}{\mathrm{d}F}$ at $45°$. (f) Boxplot of $\frac{\mathrm{d}A_c}{\mathrm{d}F}$ at $45°$.
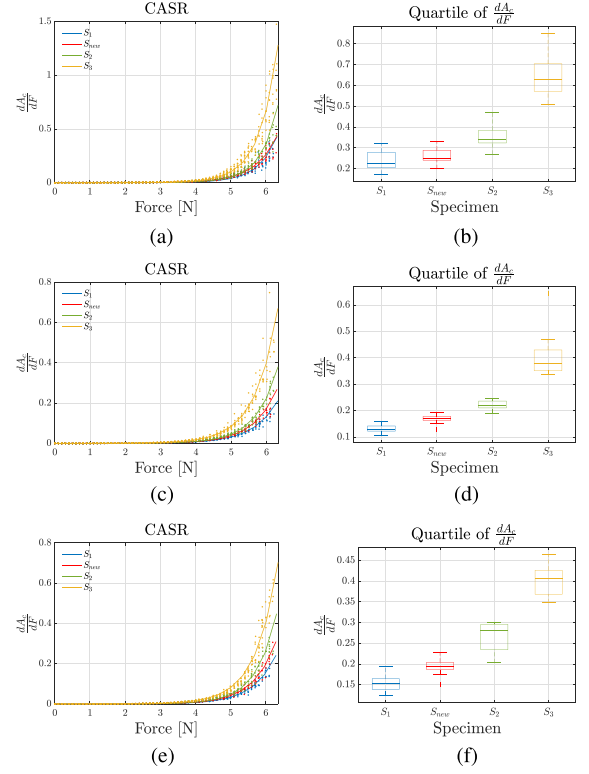

(a)

(b)

(c)

(d)

(e)

(f)

Fig. 13. S_{new} CASR discrimination based on the proposed model using constant muscular impedance values equal to the minimum, maximum, and mean values of each EMG profile. Different specimens are color-coded, respectively, S_1 in blue, S_{new} in red, S_3 in green, and S_5 in yellow. (a) Raw data and fitting of $\frac{\mathrm{d}A_c}{\mathrm{d}F}$ at $0°$ with Min_{Stiff}. (b) Boxplot of $\frac{\mathrm{d}A_c}{\mathrm{d}F}$ at $0°$ with Min_{Stiff}. (c) Raw data and fitting of $\frac{\mathrm{d}A_c}{\mathrm{d}F}$ at $0°$ with Max_{Stiff}. (d) Boxplot of $\frac{\mathrm{d}A_c}{\mathrm{d}F}$ at $0°$ with Max_{Stiff}. (e) Raw data and fitting of $\frac{\mathrm{d}A_c}{\mathrm{d}F}$ at $0°$ with $Mean_{Stiff}$. (f) Boxplot of $\frac{\mathrm{d}A_c}{\mathrm{d}F}$ at $0°$ with $Mean_{Stiff}$.

adjusted R-squared of 0.9753 in the worst case. Specifically, we obtained three fitted curves, one for each considered angle, equal to $10.21e^{-1.567x}, 14.76e-23.94x$, and $8.639e^{-58.67x}$, for $0°$, $30°$, and $45°$, respectively, where x is the CASR value. Through this relation, we estimated $K_{S_{new}}$ obtaining an estimation error equal to 3%, 3%, and 4% for $0°$ $30°$, and $45°$, respectively.

We used the same methodology to analyze the data collected during the experiments conducted under constant stiffness conditions, i.e., $Minx_{EMG}$, Max_{Stiff}, and $Mean_{Stiff}$. The statistical analysis through Bonferroni correction resulted in a p-value equal to 0.0037in the worst case of minimum stiffness, 0.0018in the worst case of maximum and mean stiffness. After that, we computed the CASR of S_{new} verifying that, different from cases with maximum and mean stiffness, using minimum stiffness does not allow discriminating S_{new} from S_1 (p-value $= 0.3799$) (Fig. 13). So, we extracted the relationship between CASR and specimens stiffness through exponential fitting in the cases of maximum and mean stiffness that resulted in an adjusted R-squared of 0.9849 and 0.9996, respectively. Exploiting the relations, we estimated $K_{S_{new}}$ obtaining an estimation error equal to 4.72% and 5% for Max_{Stiff} and $Mean_{Stiff}$ respectively.

VII. DISCUSSION

In our previous work [15], we presented results obtained considering indentation angles equal to $30°$ and $45°$. For the same new specimen S_{new}, we obtained an estimation error equal to 25% and 28%, respectively, for $30°$ and $45°$. The new results, as indicated in Table I, demonstrate that the new vision algorithm significantly improves estimating the stiffness of new and unknown objects. Indeed, the error is reduced by 18% and 15% for the two cases, respectively, making the new estimation error comparable to the one obtained in the case of indentation along the axis perpendicular to the specimen's surface. This underscores the substantial enhancement that the new algorithm provides to the proposed model-based biomimetic approach in evaluating the initial condition.

A greater improvement in estimation accuracy was achieved through the exploitation of variable stiffness palpation implemented by leveraging the studied human muscular impedance. Indeed, as shown in Table I, merging the human-like approach with the new vision algorithm, resulted in an additional reduction in the estimation error equal to 4%, and 9% for $30°$ and $45°$, respectively, surpassing the improvement achieved solely through the application of the new algorithm.
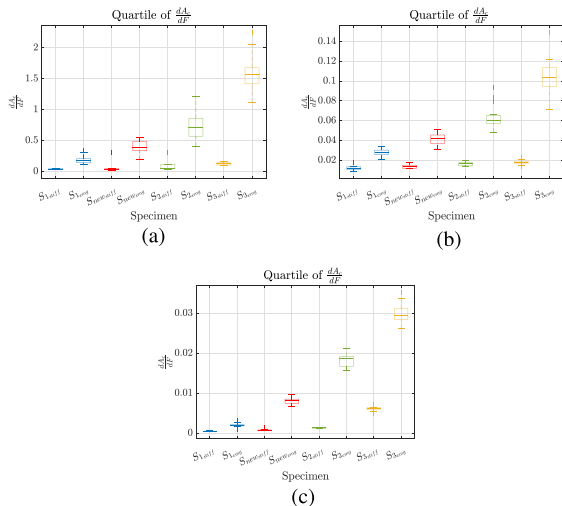
Fig. 14. Comparison of CASR discrimination obtained with both high-stiff and human-like approaches. Concerning the results that involve high-stiff palpation, we considered for $0°$ the result obtained in [15], while for $30°$ and $45°$, we reported the ones obtained with new vision algorithm and the high-stiff palpation. Different specimens are color-coded, respectively S_1 in blue, S_{new} in red, S_3 in green, and S_5 in yellow. (a) Boxplot of $\frac{dA_c}{dF}$ at $0°$. (b) Boxplot of $\frac{dA_c}{dF}$ at $30°$. (c) Boxplot of $\frac{dA_c}{dF}$ at $45°$.

If we compare the improvements achieved with both advancements on the model-based biomimetic approach, with the results obtained through the first approach proposed in [15], we observe an estimation error reduction of 3% (reduction of 50%), 22%, 24% for the three considered indentation angles.

Moreover, Fig. 14 shows a graphical representation through boxplots of the difference between results obtained with the high-stiffness approach and the human-like one in terms of values of $\frac{dA}{dF}$ obtained for each of the five examined specimens. It is evident that the human-like approach allows for a marked distinction in the values of $\frac{dA}{dF}$ with respect to the high-stiffness one. In addition, upon examining the outcomes obtained from considering the minimum, maximum, and mean values of human muscular impedance during silicone palpation, we observed the following: 1) the minimum human impedance is insufficient for effectively capturing softness information; 2) utilizing the maximum human impedance yields discrimination and stiffness estimation errors comparable to those obtained with the high-stiffness approach; and 3) while the mean human impedance ensures adequate discrimination and stiffness estimation, it falls short of the performance achieved by incorporating the entire human co-contraction profile during silicone exploration. This result suggests that humans tend to implement a dynamical adaptation of their mechanical impedance to maximize the information uptake. This highlight that incorporating an integral human muscle co-contraction strategy during specimen exploration facilitates more accurate identification of multiple object compliance levels, enhancing the device sensitivity. This demonstrates a definite improvement in our biomimetic approach.

The presented results, particularly in compliance discrimination and stiffness estimation errors, show that proposed improvements, i.e., the new vision algorithm and variable stiffness actuation, contribute significantly to the system performance, even if in distinct ways. The new vision algorithm improves the biomimetic model by enhancing the initial condition of the differential equation, enabling better compliance discrimination, especially in the case of inclined surfaces. The new variable stiffness actuation improves the exploratory process, aligning more closely with human kinesthetic input and allowing the implementation of impedance control laws for various robotic platforms. To conclude, it is worth noting that even if the new vision algorithm offers limited improvement for surfaces perpendicular to the sensor–where the previous approach already performed well–both enhancements are essential for ensuring robust, adaptable performance across different conditions, making the combination of both contributions fundamental.

VIII. CONCLUSION

In this work, we built upon our previous results, where we used a computational model of human tactile perception with the TacTip sensor for object compliance discrimination. More specifically, we strengthen our approach by proposing a new vision algorithm for a more precise estimation of the initial contact area condition, which enables correct compliance estimation also when the probing direction is other than normal to the specimen surface. More importantly, looking at the human example, we mapped human muscular co-contraction patterns extracted during object probing for softness onto a variable stiffness actuator that mimics the behavior of agonistic–antagonistic muscle. We found significant improvements with respect to our previous results obtained using a rigid actuator to indent the external items with TacTip, demonstrating that the new vision algorithm and variable stiffness actuation significantly enhance system performance.

However, our method has certain limitations, many of which we aim to address in future work. First, it relies on cutaneous sensing, which is related to soft tactile sensor surface deformation. While this allows for the estimation of softness, when probing for softness specimens that have the same CASR behavior, humans rely also on the kinesthetic perceptual component (i.e., classical force-indentation processing), whose integration with CASR computation was proven to improve the discrimination performance [49]. In addition, our approach should be tested on specimens with different elastic and hyper-elastic properties, and in conditions beyond quasi-static scenarios. To address these points, an integration of our model-based approach with data-driven methods is currently under investigation. Moreover, from the results, it is evident that higher exploration forces enhance the model performance, while lower forces result in decreased accuracy, a limitation inherent to CASR-based estimation. However, it is worth noting that these values are aligned with the force range used by humans for softness perception [48], which support the biomimicry of our approach. Nonetheless, we acknowledge that this is a limitation of our method from a mathematical and technical point of view, as well as the need for the monotonic increase of the indenting force for CASR estimation. Despite this, the results of the new model demonstrate enhanced robustness and adaptability across various exploration

conditions, opening promising scenarios for the integrated perception and grasping control of soft deformable objects with miniaturized versions of the TacTip and variable impedance human-inspired robotic hands [50]. Moreover, in the future, the integration of our method with soft optical sensor compliance control, e.g., taking inspiration from pressure-modulated optical tracking sensors for quantifying specimen stiffness during dynamic palpation [7], will also be considered.

REFERENCES

[1] C. P. Ryan, G. C. Bettelani, S. Ciotti, C. Parise, A. Moscatelli, and M. Bianchi, "The interaction between motion and texture in the sense of touch," *J. Neuriophysiol.*, vol. 126, no. 4, pp. 1375–1390, 2021, doi: 10.1152/jn.00583.2020.

[2] S. Biswas and Y. Visell, "Haptic perception, mechanics, and material technologies for virtual reality," *Adv. Funct. Mater.*, vol. 31, no. 39, 2021, Art. no. 2008186, [Online]. Available: https://onlinelibrary.wiley.com/doi/abs/10.1002/adfm.202008186

[3] M. Santello et al., "Hand synergies: Integration of robotics and neuroscience for understanding the control of biological and artificial hands," *Phys. Life Rev.*, vol. 17, pp. 1–23, 2016.

[4] B. Ward-Cherrier et al., "The TacTip family: Soft optical tactile sensors with 3D-printed biomimetic morphologies," *Soft Robot.*, vol. 5, no. 2, pp. 216–227, 2018, doi: 10.1089/soro.2017.0052 .

[5] K. Shimonomura, "Tactile image sensors employing camera: A review," *Sensors*, vol. 19, no. 18, 2019, Art. no. 3933.

[6] W. Yuan, S. Dong, and E. H. Adelson, "Gelsight: High-resolution robot tactile sensors for estimating geometry and force," *Sensors*, vol. 17, no. 12, 2017, Art. no. 2762.

[7] D. G. Raitt, M. Huseynov, S. Homer-Vanniasinkam, H. A. Wurdemann, and S.-A. Abad, "Soft-tipped sensor with compliance control for elasticity sensing and palpation," *IEEE Trans. Robot.*, vol. 40, pp. 2430–2441, 2024.

[8] N. F. Lepora, "Soft biomimetic optical tactile sensing with the tactip: A review," *IEEE Sensors J.*, vol. 21, no. 19, pp. 21131–21143, Oct. 2021.

[9] M. D. Luca, *Multisensory Softness: Perceived Compliance From Multiple Sources of Information*. Berlin, Germany: Springer, 2014.

[10] M.A. Srinivasan and R. H. LaMotte, "Tactual discrimination of softness," *J. Neuriophysiol.*, vol. 73, no. 1, pp. 88–101, 1995.

[11] W. Yuan, C. Zhu, A. Owens, M.A. Srinivasan, and E. H. Adelson, "Shape-independent hardness estimation using deep learning and a gelsight tactile sensor," in *Proc. 2017 IEEE Int. Conf. Robot. Automat.*, 2017, pp. 951–958.

[12] S. Dong, W. Yuan, and E. H. Adelson, "Improved gelsight tactile sensor for measuring geometry and slip," in *Proc. 2017 IEEE/ RSJ Int. Conf. Intell. Robots Syst.*, 2017, pp. 137–144.

[13] E. Psomopoulou, N. Pestell, F. Papadopoulos, J. Lloyd, Z. Doulgeri, and N. F. Lepora, "A robust controller for stable 3D pinching using tactile sensing," *IEEE Robot. Automat. Lett.*, vol. 6, no. 4, pp. 8150–8157, Oct. 2021.

[14] Y. Huang, M. Bianchi, M. Liarokapis, and Y. Sun, "Recent data sets on object manipulation: A survey," *Big Data*, vol. 4, no. 4, pp. 197–216, 2016.

[15] G. Pagnanelli, S. Ciotti, N. Lepora, A. Bicchi, and M. Bianchi, "Model-based compliance discrimination via soft tactile optical sensing and optical flow computation: A biomimetic approach," *IEEE Robot. Automat. Lett.*, vol. 8, no. 10, pp. 6611–6618, Oct. 2023.

[16] A. Bicchi, E. P. Scilingo, and D. De Rossi, "Haptic discrimination of softness in teleoperation: The role of the contact area spread rate," *IEEE Trans. Robot. Automat.*, vol. 16, no. 5, pp. 496–504, Oct. 2000.

[17] S. C.-H. Yang, D. M. Wolpert, and M. Lengyel, "Theoretical perspectives on active sensing," *Curr. Opin. Behav. Sci.*, vol. 11, pp. 100–108, 2016.

[18] S. J. Lederman and R. L. Klatzky, "Relative availability of surface and object properties during early haptic processing," *J. Exp. Psychol.: Hum. Percep. Perform.*, vol. 23, no. 6, 1997, Art. no. 1680.

[19] J. Konstantinova, M. Li, G. Mehra, P. Dasgupta, K. Althoefer, and T. Nanayakkara, "Behavioral characteristics of manual palpation to localize hard nodules in soft tissues," *IEEE Trans. Biomed. Eng.*, vol. 61, no. 6, pp. 1651–1659, Jun. 2014.

[20] N. Sornkarn, P. Dasgupta, and T. Nanayakkara, "Morphological computation of haptic perception of a controllable stiffness probe," *PLoS One*, vol. 11, no. 6, 2016, Art. no. e0156982.

[21] N. Sornkarn and T. Nanayakkara, "Can a soft robotic probe use stiffness control like a human finger to improve efficacy of haptic perception?," *IEEE Trans. Haptics*, vol. 10, no. 2, pp. 183–195, Apr.–Jun. 2017.

[22] Z. Wang, X. Xu, D. Yang, B. Güleçyüz, F. Meng, and E. Steinbach, "Teleoperation with haptic sensor-aided variable impedance control based on environment and human stiffness estimation," *IEEE Sensors J.*, vol. 24, no. 14, pp. 22168–22177, Jul. 2024.

[23] Z. Su, J. A. Fishel, T. Yamamoto, and G. E. Loeb, "Use of tactile feedback to control exploratory movements to characterize object compliance," *Front. Neurorobot.*, vol. 6, Jul. 2012, Art. no. 7.

[24] M. G. Catalano et al., "VSA-cubeBot: A modular variable stiffness platform for multiple degrees of freedom robots," in *Proc. 2011 IEEE Int. Conf. Robot. Automat.*, 2011, pp. 5090–5095.

[25] A. Faragasso et al., "Endoscopic add-on stiffness probe for real-time soft surface characterisation in MIS," in *Proc. IEEE 36th Annu. Int. Conf. Eng. Med. Biol. Soc.*, 2014, pp. 6517–6520.

[26] A. Bicchi, E. P. Scilingo, E. Ricciardi, and P. Pietrini, "Tactile flow explains haptic counterparts of common visual illusions," *Brain Res. Bull.*, vol. 75, no. 6, pp. 737–741, 2008, special Issue: Robotics and Neuroscience, [Online]. Available: https://www.sciencedirect.com/science/article/pii/S0361923008000117

[27] J. J. Gibson, *The Perception of the Visual World*. Cambridge, USA: Houghton Mifflin Company, 1950.

[28] J. J. Gibson, "The theory of affordances," *Perceiving, Acting Knowing: Towards Ecological Psychol./Erlbaum*, 1977.

[29] K. Nakayama and J. M. Loomis, "Optical velocity patterns, velocity-sensitive neurons, and space perception: A hypothesis," *Perception*, vol. 3, no. 1, pp. 63–80, 1974.

[30] J. J. Gibson and L. Carmichael, *The Senses Considered as Perceptual Systems*, vol. 2, no. 1. Boston, MA, USA: Houghton Mifflin, 1966.

[31] S. Baker, D. Scharstein, J. Lewis, S. Roth, M. J. Black, and R. Szeliski, "A database and evaluation methodology for optical flow," *Int. J. Comput. Vis.*, vol. 92, no. 1, pp. 1–31, 2011.

[32] B. K. Horn and B. G. Schunck, "Determining optical flow," *Artif. Intell.*, vol. 17, no. 1-3, pp. 185–203, 1981.

[33] D. Fleet and Y. Weiss, "Optical Flow Estimation," in *Handbook of Mathematical Models in Computer Vision*. Berlin, Germany: Springer, 2006, pp. 237–257.

[34] A. Bruhn, J. Weickert, and C. Schnörr, "Lucas/Kanade meets Horn/Schunck: Combining local and global optic flow methods," *Int. J. Comput. Vis.*, vol. 61, no. 3, pp. 211–231, 2005.

[35] J.-Y. Bouguet et al., "Pyramidal implementation of the affine Lucas Kanade feature tracker description of the algorithm," *Intel Corporation*, vol. 5, no. 1-10, 2001, Art. no. 4.

[36] S. Baker and I. Matthews, "Lucas-Kanade 20 years on: A unifying framework," *Int. J. Comput. Vis.*, vol. 56, pp. 221–255, 2004.

[37] R. Cipolla and A. Blake, "Surface orientation and time to contact from image divergence and deformation," in *Proc. Eur. Conf. Comput. Vis.*, 1992, pp. 187–202.

[38] N. Herzig, P. Maiolino, F. Iida, and T. Nanayakkara, "A variable stiffness robotic probe for soft tissue palpation," *IEEE Robot. Automat. Lett.*, vol. 3, no. 2, pp. 1168–1175, Apr. 2018.

[39] C. Della Santina et al., "The quest for natural machine motion: An open platform to fast-prototyping articulated soft robots," *IEEE Robot. Automat. Mag.*, vol. 24, no. 1, pp. 48–56, Mar. 2017.

[40] M. Garabini, C. D. Santina, M. Bianchi, M. Catalano, G. Grioli, and A. Bicchi, "Soft robots that mimic the neuromusculoskeletal system," in *Proc. Converging Clin. Eng. Res. Neurorehabil. II: Proc. 3rd Int. Conf. NeuroRehabil.*, Segovia, Spain, 2017, pp. 259–263.

[41] A. G. Feldman, "Once more on the equilibrium-point hypothesis (λ model) for motor control," *J. motor Behav.*, vol. 18, no. 1, pp. 17–54, 1986.

[42] S. Fani et al., "Assessment of myoelectric controller performance and kinematic behavior of a novel soft synergy-inspired robotic hand for prosthetic applications," *Front. Neurorobot.*, vol. 10, 2016, Art. no. 11.

[43] A. Z. Hajian and R. D. Howe, "Identification of the mechanical impedance at the human finger tip," *ASME. J. Biomech Eng.*, vol. 119, no. 1, pp. 109–114, 1997.

[44] K. Akazawa, T. Milner, and R. Stein, "Modulation of reflex emg and stiffness in response to stretch of human finger muscle," *J. Neuriophysiol.*, vol. 49, no. 1, pp. 16–27, 1983.

[45] G. Kamen and D. A. Gabriel, *Essentials of Electromyography*. Human Kinetics, 2009.

[46] B. Delhaye, P. Lefevre, and J.-L. Thonnard, "Dynamics of fingertip contact during the onset of tangential slip," *J. Roy. Soc. Interface*, vol. 11, no. 100, 2014, Art. no. 20140698.

[47] S. Ciotti, T. Sun, E. Battaglia, A. Bicchi, H. Liu, and M. Bianchi, "Soft tactile sensing: Retrieving force, torque and contact point information from deformable surfaces," in *Proc. 2019 Int. Conf. Robot. Automat.*, 2019, pp. 4290–4296.
[48] S. Zhang et al., "Texture design for light touch perception," *BioSurface Biotribol.*, vol. 3, no. 1, pp. 25–34, 2017.
[49] E. P. Scilingo, M. Bianchi, G. Grioli, and A. Bicchi, "Rendering softness: Integration of kinesthetic and cutaneous information in a haptic device," *IEEE Trans. Haptics*, vol. 3, no. 2, pp. 109–118, Apr.–Jun. 2010.
[50] C. J. Ford et al., "Tactile-driven gentle grasping for human-robot collaborative tasks," in *Proc. 2023 IEEE Int. Conf. Robot. Automat.*, 2023, pp. 10394–10400.

Giulia Pagnanelli (Graduate Student Member, IEEE) received the B.S. degree in biomedical engineering and the M.S. (cum laude) degree in robotics and automation engineering, in 2020 and 2022, respectively, from the University of Pisa, Pisa, Italy, where she is currently working toward the Ph.D. degree in information engineering and robotics with the Department of Information Engineering and the Research Center "E. Piaggio."

Her research interests include the design and validation of wearable haptic devices and related control feedback interfaces for human–robot interaction in robotic surgery, prosthetics, and robotic grasping and manipulation fields.

Lucia Zinelli (Student Member, IEEE) received the M.S. (cum laude) degree in robotics and automation engineering, in 2023, from the University of Pisa, Pisa, Italy, where she is currently working toward the Ph.D. degree in information engineering and robotics with the Department of Information Engineering and the Research Center "E. Piaggio".

Her research interests include human tactile interaction modeling, wearable tactile sensing systems, and haptic-interfaces.

Nathan Lepora (Member, IEEE) received the B.A. degree in mathematics and the Ph.D. degree in theoretical physics from the University of Cambridge, Cambridge, U.K., in 1992 and 1996, respectively.

He is currently a Professor of robotics and AI with the University of Bristol, Bristol, U.K. He leads the Dexterous Robotics Group, Bristol Robotics Laboratory.

Dr. Lepora is a recipient of a Leverhulme Research Leadership Award for "A biomimetic Forebrain for Robot Touch," and was co-editor of the book *Living Machines* that won the 2019 BMA Medical Book Awards (basic and clinical sciences category). His research team won the "University Research Project of the Year" at the 2022 Elektra Awards.

Manuel Catalano (Member, IEEE) received the B.S. and M.S. degrees in mechanical engineering and the Ph.D. degree in robotics from the University of Pisa, Pisa, Italy, in 2006, 2008, and 2013, respectively.

He is currently a Researcher with the Italian Institute of Technology, Genoa, Italy, and a collaborator of the Research Center "E. Piaggio," University of Pisa. His research interests include the design of soft robotic systems, human–robot interaction, and prosthetics.

Dr. Catalano was the recipient of the Georges Giralt Ph.D. Award in 2014, the prestigious annual European award given for the best Ph.D. thesis by euRobotics AISBL.

Antonio Bicchi (Life Fellow, IEEE) received the Ph.D. degree in mechanical engineering from the University of Bologna, Bologna, Italy, in 1988.

He is currently a Scientist interested in robotics and intelligent machines. He holds a chair in Robotics with the University of Pisa, Pisa, Italy, and leads the Soft Robotics Laboratory, Italian Institute of Technology, Genova, Italy. He is also an Adjunct Professor with Arizona State University, Tempe, AZ, USA.

Dr. Bicchi's work is the recipient of many international awards and has earned him four prestigious grants from the European Research Council (ERC). He launched initiatives such as the WorldHaptics conference series, *IEEE Robotics and Automation Letters*, and the Italian Institute of Robotics and Intelligent Machines.

Matteo Bianchi (Member, IEEE) received the Ph.D. (with International Doctorate qualification) degree in automatics, robotics and bio-engineering from the University of Pisa, Pisa, Italy, in 2012.

He is currently an Associate Professor with the Department of Information Engineering (DII) and the Bioengineering and Robotics Research Centre "E. Piaggio,' Università di Pisa, Pisa, Italy. From 2015 to 2023, he was a clinical Research Affiliate with Mayo Clinic, Rochester, USA. From 2017 to 2022, he served as co-Chair of the RAS Technical Committee on Robot Hands, Grasping and Manipulation and from 2018 to 2021, as Vice-Chair for Information and Dissemination of the RAS Technical Committee on Haptics. He acts as the Principal Investigator of national and EU grants, and research contracts with companies in the field of human–machine interaction. He has authored or coauthored more than 150 peer-reviewed contributions. His research interests include haptics and robotic hands.

Prof. Bianchi is a Member of the editorial/organizing board of several international conferences and journals.